Journal of Electrostatics 115 (2022) 103654

Contents lists available at ScienceDirect

Journal of Electrostatics

journal homepage: www.elsevier.com/locate/elstat

Spray characteristics of an air-assisted electrostatic atomiser

Antoni Brentjes *, Bart Jansen, Artur K. Pozarlik

Department of Thermal and Fluid Engineering, University of Twente, Enschede, The Netherlands

ARTICLE INFO

Keywords:
Electrostatic spray
Two-fluid atomiser
Droplet/particle image analysis
Droplet size distribution
Sauter Mean Diameter

ABSTRACT

The spray characteristics of an air-assisted electrostatic atomiser are experimentally investigated using a shadowgraphy particle/droplet image analysis (PDIA) technique. Tests are conducted for varied rates of liquid- and airflow, with and without a voltage applied to the nozzle electrode. The found droplet sizes neatly match the Rosin–Rammler distribution, and an expression for the mean diameter as a function of the flow rates is given. Notably, the electrode voltage (up to 40 kV) has no measurable impact on the droplet size and velocity, and the energy efficiency of the sprayer is found to decrease with increases in both liquid- and airflow.

1. Introduction

Electrostatic charging of sprays is a proven method for improving the effectiveness of various spraying processes. Its use is well established in applications such as paint spraying [1], powder coating [2], agricultural sprays [3], flue gas scrubbing [4], and recently drew significant interest in disinfectant application [5]. Arguably, the two primary benefits of charged particles are their attraction to (grounded) objects, and their mutual repulsion. These properties result in better transfer efficiency of coatings, and better dispersion of aerosols. In the present research we work towards a new application of charged sprays: efficient spray-chilling in the meat industry. Spraying carcasses with water during the initial chilling is known to reduce drying and provide additional evaporative cooling [6]. Using charged instead of conventional sprays will reduce water consumption and overspray, which can otherwise result in high cost and hygiene problems [7].

To design an efficient and effective electrostatic spray chilling system, an appropriate sprayer type must be selected. For industrial applications with moderate liquid flow rates and a preference for droplet sizes below 100 μm, three main types of atomiser are typically used. Single fluid pressure atomisers with inductive charging [8] are mechanically simple and economical. However, these produce relatively large droplets, unless operated at pressures upward of 10 bar [9]. Pneumatic or air-assisted electrostatic atomisers can produce fine sprays while operating at pressures around 2 bar [10,11], without much added complexity. This comes at the cost of an increased energy consumption, in the form of compressed air. Finally, (electrostatic-assisted) rotary bell atomisers, despite their high cost and complexity, have become popular in automotive painting, since they produce highly uniform and high quality surface coatings [12].

Based on these general characteristics, an air-assisted atomiser offers the most flexible and economical option. However, relatively little recent experimental data is available on the performance of such atomisers [13], as most spray-painting research has focused on rotary bell sprayers. This is unfortunate, since an accurate and detailed characterisation of the spray is necessary to proceed with numerical design studies for an electrostatic spray chilling system [14]. Therefore, in the present research, we will perform an experimental study of the characteristics of an electrostatic air-assisted atomiser. A high-speed shadowgraphy method [15] is used to obtain both droplet size and velocity data, both of which are necessary to later reproduce the spray in a Lagrangian numerical simulation.

2. Theory

Many different models and types of sprayer exist, operating on different principles and mechanisms. In order to keep our discussion of theory concise, we first introduce the design of the investigated sprayer, and then examine relevant results from literature.

2.1. Sprayer design

A commercial electrostatic air spray gun (Graco type LC2028) is selected for the present research. Although designed and typically used for spraying paint, appropriately sized nozzles and electrically isolated liquid feed systems are available to allow spraying with water. A schematic sketch of the nozzle head is shown in Fig. 1, with major components highlighted. Photo's of the sprayer in operation are shown in Figs. 2(b) and 2(c).

* Corresponding author.
E-mail addresses: a.brentjes@utwente.nl (A. Brentjes), b.a.jansen@student.utwente.nl (B. Jansen), a.k.pozarlik@utwente.nl (A.K. Pozarlik).

https://doi.org/10.1016/j.elstat.2021.103654
Received 22 July 2021; Received in revised form 26 November 2021; Accepted 26 November 2021
Available online 4 January 2022

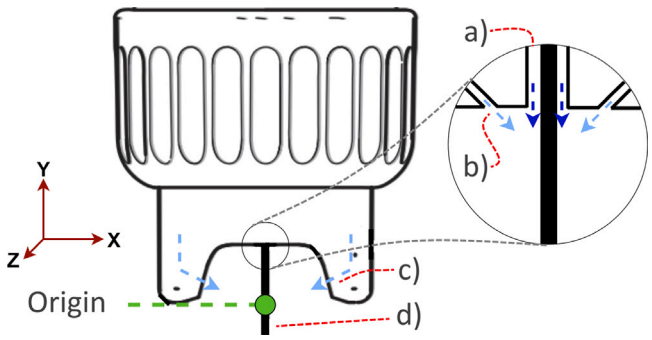

Fig. 1. Schematic drawing of the investigated sprayer nozzle. Water is injected through annular nozzle (a), surrounding a conductive needle electrode (d). "Primary" air jets (b) initiate the breakup of the water surface, while "secondary" air jets (c) assist the atomisation process and shape the spray into a flat fan.

A cylindrical electrode is located centrally in the nozzle, which conductively charges the spray liquid when a high voltage is applied. The electrode is surrounded by an annular nozzle through which the spray liquid is supplied. Several circular 'primary' air nozzles surround the liquid nozzle, aimed axially and inward to destabilise the liquid jet. Two 'secondary' air nozzles are located in the horns of the sprayer head, creating jets that impinge on the liquid at a near perpendicular angle. This model of sprayer head produces a flat fan-like spray profile, which may be adjusted by to a certain degree by varying the primary and secondary airflow. For that reason the primary and secondary air jets are also referred to as "atomisation" and "shaping" air, but in practice both play a role in the atomisation process. In standard operating conditions the liquid and air are supplied at 0.2 MPa gauge pressure, corresponding to 180 ml/min liquid flow and 425 sl/min air flow.

2.2. Spray formation

Anestos et al. [10], McCarthy and Senser [11], and Ye and Pulli [13] have previously investigated similar models of sprayer. However, the first two works are focused on the electrical properties of the spray. Anestos and Ye also offer a brief discussion of the droplet size distribution, but none of the authors go into depth regarding the spray breakup mechanism or the scaling with varying operating conditions.

For sprayers with high air velocities and a relatively obtuse angle between air and liquid, Lefebvre [9,16] suggested the so-called prompt breakup mechanism. This mechanism is characterised by a violent disruption of the initial liquid jet or sheet, and generates droplets in a relatively wide size-range. Lefebvre proposed a relation for the Sauter mean diameter of the produced droplets based on a balance of free surface energy and the kinetic energy of the atomising air, given as Eq. (1). Considering the design of the used atomiser, this physics-based relation seems to give the most appropriate estimate for our case.

$$SMD = \frac{3}{\left[\frac{2}{D_j} + \frac{C\rho_L U_A^2 \dot{m}_a}{4\sigma \dot{m}_w}\right]} \tag{1}$$

Here, D_j represents the diameter of the initial liquid jet and ρ_w, $\dot{m}_w$, and σ the density, mass-flow, and surface tension of the liquid. U_a and $\dot{m}_a$ are the velocity and mass-flow of the atomising air, and C is the energy efficiency of the atomisation process (expected to be in the order of 10^{-4} [9]).

2.3. Electric potential

In addition to the liquid and air flow, electrostatic effects can also influence spray formation. Applying an electric field to a conductive liquid spray, whether by means of an induction electrode or by direct charging, will cause charges to accumulate on the surface of the liquid. The mutual repulsion of these charges then counteracts the liquid's surface tension. If sufficient voltage is applied to a liquid droplet or filled capillary, the surface can form a Taylor cone, emitting a jet or spray plume from its tip. Increasing the applied voltage generally results in smaller droplets being produced in such electrosprays [17]. However, capillary electrosprays operate at far lower flow rates than the sprayer currently being investigated. Studies investigating high-flowrate atomisers (including pressure-, air assisted- and rotary bell atomisers) generally do not report whether or not the electric potential influences the droplet size distribution.

In order to compute the influence of electrostatic forces on a liquid's surface, the local surface charge and the local electric field must be known. For relatively simple sprayers, such as cone-jet electrosprays, these have been computed using numerical models [18,19]. The breakup region of our air-assisted electrostatic atomiser is highly unsteady, due to the high velocity air impinging on the water jet, leading to far more complicated surface shapes. At present, no high resolution analyses of the flow in this breakup region, nor of the surface charge distribution and electric field exist. Lacking such local data, we can only rely on global balances to estimate the effect of charge on the spray formation.

The first global parameter we can use to estimate the relevance of electrostatic effects in an air-assisted atomiser is the energy balance. Anestos et al. [10], and McCarthy and Senser [11], investigated similar air-assisted electrostatic atomisers, and measured electrical currents between (approximately) 15 and 110 μA for supply potentials between 60 and 110 kV. This corresponds to an electric power input ranging between 1 and 12 W. The primary atomisation air-jets in the investigated sprayers consume around 5 g/s of air, at a supply pressure of 0.4 MPa, corresponding to 250 W of pneumatic power. This suggests that the atomisation process will be dominated by fluid dynamic effects, rather than electrostatic effects. However, considering the expected efficiency of the pneumatic atomisation process is in the order of 10^{-4}, this cannot be concluded with certainty.

A second global measure to consider is the specific charge of the spray droplets. Shrimpton and Laoonual [20] formulate the effect of the surface charge on a spherical droplet's cohesion as a compensated surface tension: $\sigma^* = \sigma - Q^2/(8\pi^2\epsilon_0 D^3)$. The charge for which the effective surface tension becomes zero is called the Rayleigh charge limit. Any droplet with a charge in excess of that limit will immediately disintegrate in a coulomb explosion. Lesser amounts of charge will not directly cause droplet breakup, but by reducing the effective surface tension and increasing the effective Weber number they will still contribute to this process. We can again estimate the expected magnitude of this effect by looking at the results of Anestos et al. [10], and McCarty and Senser [11]. The droplet charge levels measured by them correspond to less than 15% of the Rayleigh limit, which would result in a 2% decrease of the effective surface tension. This suggests the electric charge will have a relatively minor effect on the size and stability of the droplets after primary and secondary breakup. Since the effect scales with droplet volume given a constant specific charge, it might still influence the formation of large droplets and ligaments in the primary breakup region.

Finally, charged sprays are known to have increased self-dispersion compared to uncharged sprays. However, as can be seen in numerical simulation results [14], the effect of electric charge on droplet trajectories only becomes dominant at some distance from the sprayer. Based also on the energy balance, it should be expected that the droplet trajectories near the sprayer are dominated by aerodynamic and inertial forces.

3. Methodology

A direct optical imaging technique is used to characterise the spray and determine the droplet size and velocity distribution. Typically

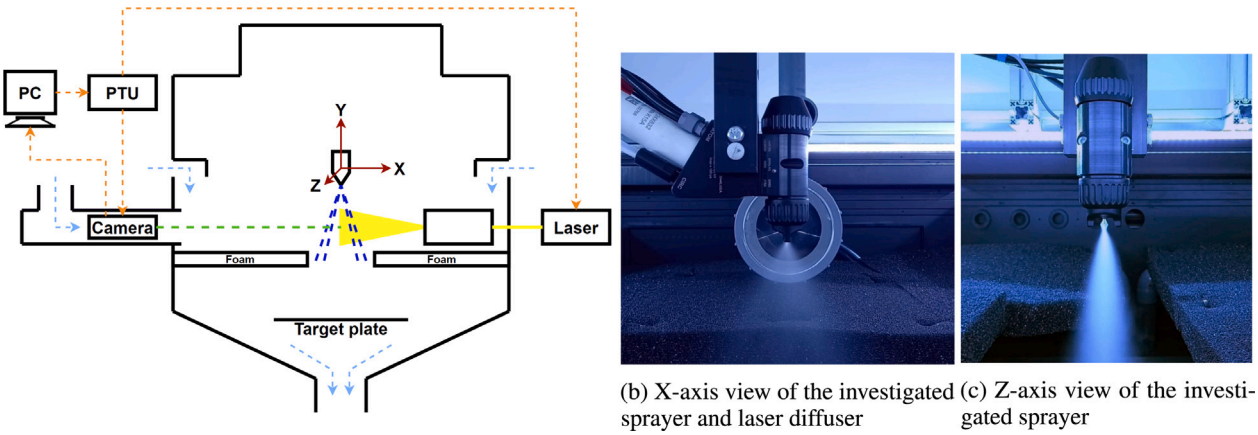

(b) X-axis view of the investigated sprayer and laser diffuser (c) Z-axis view of the investigated sprayer

Fig. 2. The PDIA setup consists of a high speed camera and a pulsed laser connected to a diffuser. The sprayer is mounted between light source and camera, allowing shadowgraphs of the spray to be taken in quick succession. The laser and camera are driven by a Programmable Timing Unit, controlled by a desktop computer. A darkened and ventilated enclosure with internal baffles prevents moisture and laser light from escaping the setup.

referred to as particle/droplet image analysis (PDIA) or particle shadowgraphy, this method uses a high-resolution camera and pulsed laser illumination to record shadow images of the spray. Image processing software is used to find droplets and determine their size, position and roundness, while droplet velocities are found by correlating two images taken in rapid succession. This imaging setup was initially constructed by Sallevelt [15], who also describes the calibration procedure and accuracy in detail.

3.1. Measurement setup

Fig. 2(a) shows a schematic overview of the experimental setup. The primary components are a SX-9M (LaVision) high speed camera, and a frequency-doubled Nd:YAG pulsed laser for illumination. The investigated sprayer is mounted on a traverse mechanism, so that the spray cone can be moved through the field of view of the camera. The laser and camera are driven by a Programmable Timing Unit, which communicates with a PC running LaVision's DaVis software (version 10.1.0). A grounded stainless steel plate is mounted approximately 250 mm below the sprayer nozzle, to act as a target for the spray. The test rig is enclosed in a grounded and light-sealed metal chamber, with ventilation and foam baffles installed to prevent recirculation of droplets and fogging of the optics.

The used camera has a resolution of 3360 by 2712 pixels, with a long-distance microscope (Questar QM1) fitted to obtain a 5 by 4.04 mm field of view, corresponding to 1.489 μm per pixel. A pulse delay of 1.5 μs is used between image pairs, such that the average droplet is displaced by a distance approximately equal to its own diameter, as recommended by LaVision [21]. With a laser pulse duration of 6 ns the droplet displacement during the pulse is far less than one pixel unit, and high quality sharp images are obtained.

3.2. Measurement procedure

Following initial setup and calibration, measurements were conducted at different locations in the spray cone and at different process parameters. For each measurement, the sprayer was translated to the appropriate location and the air pressure, water pressure, and electrode voltage were set. The sprayer was then enabled, and after a two second delay to allow transient start-up effects to dissipate the imaging sequence was started. For each datapoint, 120 pairs of images were taken, over the course of 15 s. This was found to be sufficient to converge the statistical properties of the spray. Since post-processing and the computation of the spray statistics was too expensive to carry out in real time, the image count was taken in excess of the minimum, and statistical convergence was evaluated during post-processing.

Table 1
Tested range of water and air flow rates, with corresponding supply pressures.

Pressure [bar gauge]	Water flow rate [ml/min]	Air flow rate [sl/min]
1.5	145	318
2.0	180	425
2.5	215	533
3.0	245	640
3.5	268	–
4.0	290	–

The sprayer parameters were controlled using mechanical pressure regulators for both water and airflow. The water flow rate was determined by operating the sprayer for one minute at each different water pressure setting, and measuring the difference in the weight of the supply tank. The air flow rate was determined using a Brooks MT3809 gas flow meter. The electric potential and current were recorded from the electronic controller integral to the Graco spray system.

3.2.1. Investigated variables and range

The investigated sprayer can operate at air and liquid pressures between 0 and 7 bar (gauge). The recommended range however is between 1.5 and 4 bar, so that range is used in our investigation. The flow rates of air and water for the tested pressures are given in Table 1. The voltage supply in the sprayer head is rated up to 60 kV, but can only reach this voltage at very low current draw. An upper limit of 40 kV was used during the present measurements, which could be reliably maintained under all flow settings.

Measurements were taken along the principal axis of the sprayer to find the primary spray breakup point, starting at 7.5 mm downstream of the nozzle. Measurements were also taken along the long and short lateral axis of the spray fan, to find its width and thickness profile. An exhaustive sweep of the operating conditions was done at a location 25 mm downstream of the nozzle, forming the main dataset.

3.3. Image and data processing

The LaVision Davis software with the ParticleMaster Shadow extension was used for processing the images. This software recognises individual particles within each image, and records their locations, sizes and the image luminance gradient of their boundary (i.e. edge sharpness). It then correlates the data within each image pair, pairing detections of the same particle to determine their velocity. Following this basic analysis, the data is filtered on several criteria.

First, detected particles are filtered on the image luminance gradient of their boundary (simply referred to as Gradient Intensity by

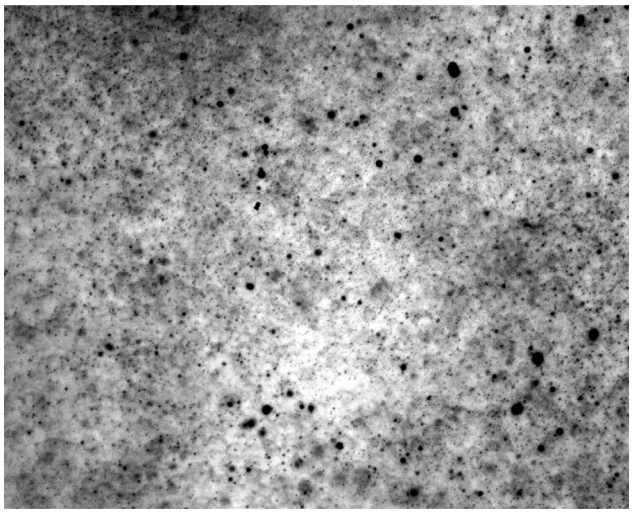

Fig. 3. A shadowgraph taken during the experiment, at a water flow rate of 180 ml/min and an air flow rate of 425 sl/min, 25 mm below the injector. Droplets in the focal plane appear dark and sharp, whereas droplets outside the focal plane appear grey and hazy.

Sallevelt [15]). Low thresholds increase the effective depth of field, but also increase the measurement error. The filter threshold was set such that the depth of field for the SMD droplet size at default atomiser settings was 1 mm. A statistical weighting factor was calculated for each detected droplet to account for the size dependent depth-of-field and edge-exclusion effects.

The results were then scanned for repeat detections indicating dirt/dust specs on lens or sensor. Velocity data was filtered, and values deviating from the mean by more than four standard deviations were considered to be incorrect pairings, and the droplets in question were decorrelated.

4. Results

Fig. 3 shows a snapshot of the spray taken by the shadowgraphy camera. Compared to the images shown by Sallevelt et al. [15], this spray is more dense and appears to have a wider droplet size range. Furthermore, the snapshot has a cloudy appearance, caused by the presence of droplets outside the focal plane, due to the thick and solid nature of the spray cone.

Since a substantial amount of the collected data is redundant with respect to the final conclusions of this article, only the portion of the data that offers unique insights is presented.

4.1. Spray characteristics

In order to give meaningful conclusions about the spray characteristics, they must be measured and compared at a location in the spray cone where the primary breakup process is complete. At this point all spray droplets should have become roughly spherical, and the statistical spray properties should no longer dramatically change as a function of downstream distance (y). Sallevelt [15] proposes a useful metric for the former criterion: the so-called Normalised Ligament Area (NLA). This is defined as the ratio of the area of all "ligaments" present in the spray image, divided by the total area taken up by liquid. In this context, a ligament is defined as any detected object where the roundness parameter $4\pi A_c/p^2$ is smaller than 0.25. Here A_c denotes the cross-sectional area of the object and p the perimeter.

Fig. 4(b) shows the normalised ligament area as a function of downstream distance for various rates of water flow ($\dot{V}_w$) and airflow ($\dot{V}_a$). Fig. 4(a) similarly shows the Sauter Mean Diameter. For most values of the air- and water flow rate, the SMD and NLA asymptotically decrease with downstream distance. The final SMD increases with increasing water flow rate, and decreases with increasing air flow rate, as expected based on the theory of prompt atomisation. The rate of decrease of the NLA similarly appears to scale with the specific atomisation energy. Based on the low NLA and stabilised SMD we choose a downstream distance of 25 mm as suitably representative location to study the spray properties in detail.

Two observations from Fig. 4 seem anomalous or counter-intuitive. For a water flow rate of 290 ml/min, the SMD appears to initially increase with downstream distance. This may be attributed to the limitations of the image-analysis software. At such a high water flow rate large irregular "blobs" of water are still present at 7.5 mm from the sprayer nozzle. These irregular shapes are not properly recognised, and therefore not taken into account when calculating the SMD. This causes the reported SMD to be smaller than the actual SMD at that point in the spray cone. Furthermore, the results for the charged spray are virtually indistinguishable from the uncharged results, suggesting that electrostatic effects do not play a significant role in the atomisation process (see also Fig. 6).

4.1.1. Droplet size distribution

Figs. 5(a) through 5(d) show histograms of the droplet sizes measured at 25 mm downstream of the nozzle, for various water and air flow rates. A Rosin–Rammler distribution (Eq. (2)) is fitted to the measured data using a least-squares method. This fitted distribution is plotted in the same figures for comparison, and the fit parameters and Sauter mean diameter are given.

$$Q = 1 - e^{-\left(\frac{d}{d_0}\right)^N} \qquad \frac{\mathrm{d}Q}{\mathrm{d}d} = N\frac{d^{N-1}}{d_0^N}e^{-\left(\frac{d}{d_0}\right)^N} \tag{2}$$

Here Q represents the volume fraction of liquid contained by droplets smaller than d, d_0 is a reference diameter, and N a spread exponent.

Although slightly underrepresenting the top end of the size range, which is a common complaint according to Lefebvre [9], the Rosin–Rammler distribution fits the collected data fairly well. The reference diameter increases with increasing water flow rate and decreases with increased air flow rate, as expected. Contrary to initial expectation, the spread factor varies along with the reference diameter. Larger average droplet sizes correlate with not just a wider absolute size spread, but also a wider relative size spread. Comparing the data for all tested cases, we find a quantitative scaling of $N \propto d_0^{-0.38}$. The range of the observed spread factor, 1.4–2.5, matches Lefebvre's [16] observations for prompt atomisation.

4.1.2. Droplet size and velocity variation

Figs. 6(a) and 6(b) show the variation of the Sauter Mean Diameter and the mass averaged droplet velocity of the spray with varying air- and water flow rates. The SMD is seen to increase with increased water flow rate, and decrease with increasing air flow rate. The opposite pattern is seen for the droplet velocity, owing to the fact that the injected air contributes far more momentum than the injected water. The water jet velocity is less than 20 m/s, whereas the air is injected at gauge pressures exceeding 1.5 bar, resulting in locally supersonic flow.

Again there is no apparent difference between the characteristics of the charged and uncharged sprays. The only substantial deviation occurs in the measured (mass averaged) droplet velocity at minimum water flow and maximum airflow. Considering the entire dataset, we assume this deviation to be a statistical outlier rather than a true physical effect.

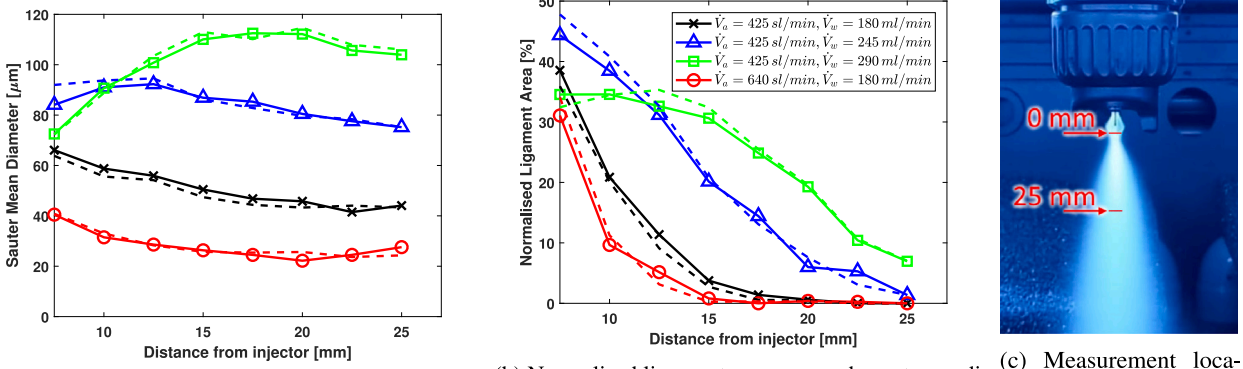

(a) Sauter mean diameter versus downstream distance (b) Normalised ligament area versus downstream distance (c) Measurement locations in reference to the sprayer

Fig. 4. Sauter mean diameter and normalised ligament area measured along the principal spray axis. Uncharged spray results plotted with solid lines, charged (40 kV) results with dashed lines. Breakup length increases with increasing water flow rate and decreasing air flow rate.

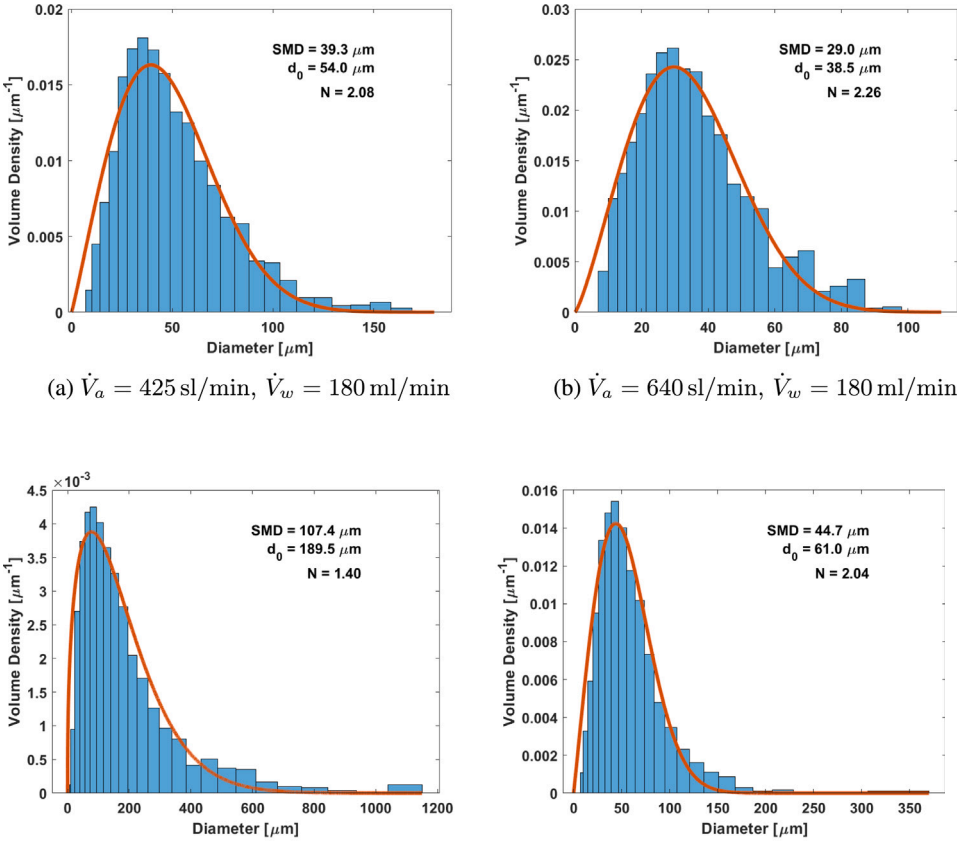

(a) $\dot{V}_a = 425\,\mathrm{sl/min},\ \dot{V}_w = 180\,\mathrm{ml/min}$ (b) $\dot{V}_a = 640\,\mathrm{sl/min},\ \dot{V}_w = 180\,\mathrm{ml/min}$

(c) $\dot{V}_a = 425\,\mathrm{sl/min},\ \dot{V}_w = 290\,\mathrm{ml/min}$ (d) $\dot{V}_a = 640\,\mathrm{sl/min},\ \dot{V}_w = 245\,\mathrm{ml/min}$

Fig. 5. Droplet size distributions at 25 mm downstream of the nozzle, for different rates of water- and airflow. Droplet size increases with increasing water flow rate and decreasing air flow rate. A narrower distribution (i.e. high spread parameter N) is seen at lower Sauter Mean Diameters and vice versa.

4.2. Effects of electrode potential

While the presented results show no effect of the electrode potential on the mean spray properties, this does not exclude the possibility that electrostatic effects influence the droplet size distribution. Fig. 7 shows the droplet size distributions of sprays generated at different voltages, while the air- and water flow rates were kept constant.

The results show that the droplet size distribution does not change significantly in response to changes in the electrode potential. Neither the Sauter mean diameter nor the spread factor N show a clear directional trend, and the range of both parameters is within the expected statistical variance.

The one variable that is significantly affected by the electrode potential is the spray current. This is measured at the high voltage supply, and is plotted in Fig. 8. The current scales linearly with the supplied potential, and does not vary with different air- and water flow rates within the investigated range, matching our theoretical expectations [22]. Unfortunately, given the integrated nature of the spraying system, we could not effectively isolate the actual spray current from

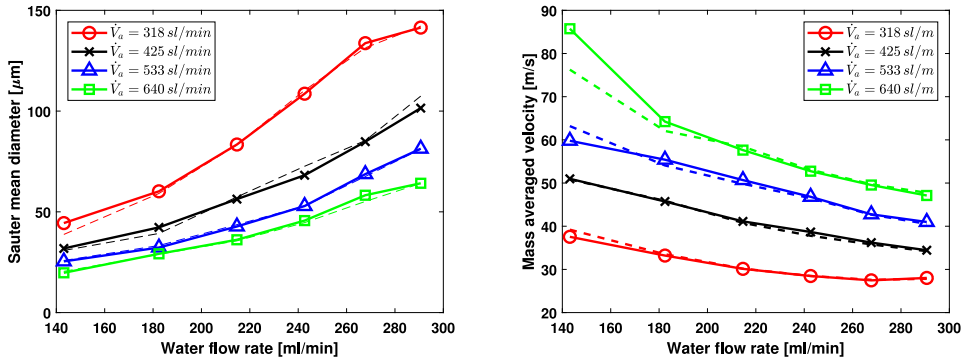

(a) Sauter mean diameter for varying air and water flow rate

(b) Mass averaged droplet velocity for varying air and water flow rate

Fig. 6. Sauter mean diameter and mass averaged droplet velocity measured 25 mm downstream of the nozzle. Uncharged spray results plotted with solid lines, charged (40 kV) results with dashed lines. Mass averaged droplet velocity increases with increasing air flow rate and decreasing water flow rate. Sprayer voltage has no apparent influence on either Sauter mean diameter or mass averaged droplet velocity.

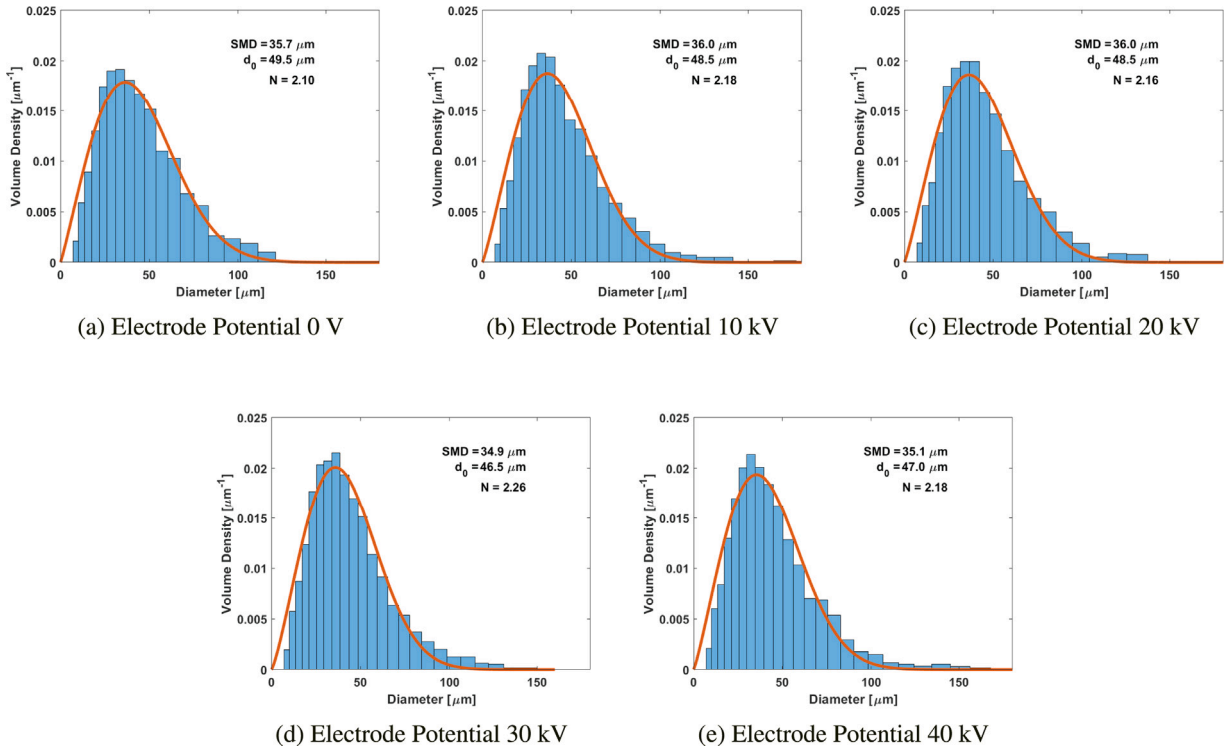

(a) Electrode Potential 0 V

(b) Electrode Potential 10 kV

(c) Electrode Potential 20 kV

(d) Electrode Potential 30 kV

(e) Electrode Potential 40 kV

Fig. 7. Droplet size distributions at 25 mm downstream of the nozzle, for different electrode potentials. The air and water flow rates are kept constant at 475 sl/min and 180 ml/min respectively. No substantial differences or trend can be observed for the mean diameter or distribution shape as a function of electrode potential.

current leakage inside the sprayer and water supply. The measured current therefore only gives us an upper bound of the specific charge of the spray. This upper bound ranges between 3.8 mC/kg and 7.6 mC/kg at an electrode potential of 40 kV, for the water flow rates given in Table 1. These values closely match those measured by Anestos et al. [10] with a similar sprayer, leading us to believe that the amount of leakage current is relatively minor.

4.3. Scaling laws

In Fig. 9 we compare our measured diameters to Lefebvre's [16] prediction for prompt atomisation (Eq. (1)). The value of the efficiency constant C is taken as 5×10^{-5}, on the low end of the estimate provided by Lefebvre. Here, it is immediately obvious that the scaling with water flow rate does not match the data. The measured Sauter Mean Diameter increases faster with increasing water flow rate than the theory predicts, implying that the energy efficiency of the atomiser decreases with increasing flow. The scaling with air flow rate is closer, but the error here also implies a decrease in energy efficiency with increasing flow.

This behaviour, although not initially expected, makes practical sense. The investigated sprayer nozzle is an external-mixing type, which means that the mixing region is surrounded by ambient air. Without confinement of the mixing region, increasing the air flow rate through the jets will cause progressively more mixing with the ambient air, losing energy in the process. Increasing the flowrate of water increases the length of the mixing and spray breakup region (as also seen in

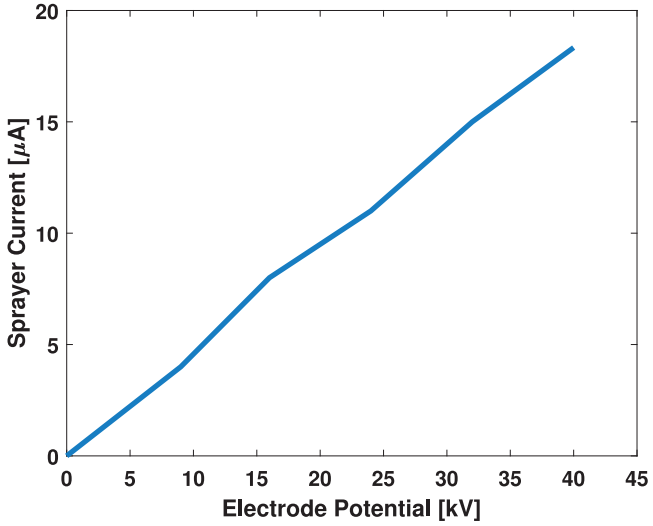

Fig. 8. Spray current as a function of electrode potential. The measured current scales linearly with the applied potential, and is constant with respect to the air and water flow rates within the investigated range.

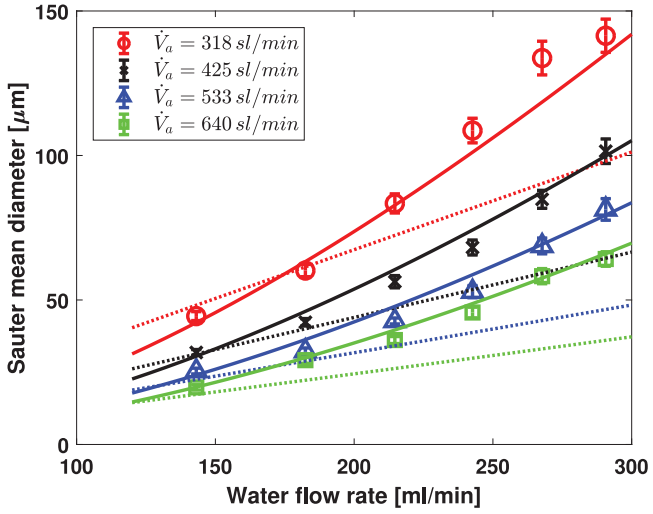

Fig. 9. Scaling laws for Sauter mean diameter compared to measurement results. Dotted lines for constant efficiency (Eq. (1)), solid lines for variable efficiency (Eq. (3)).

Fig. 4(b)), which then also increases the size of the ambient mixing region where energy is lost.

$$SMD = \frac{3}{\left[\frac{2}{D_j} + \frac{F\rho_L U_A^2 \dot{m}_a}{4\sigma \dot{m}_w}\right]} \quad \text{with} \quad F = \hat{C}\dot{m}_w^{-0.7}\dot{m}_a^{-0.4} \tag{3}$$

An improved fit on the data can be obtained with a simple power law for the energy efficiency of the sprayer, given as Eq. (3), and also plotted in Fig. 9. An efficiency function $F(\dot{m}_w, \dot{m}_a)$ is introduced, replacing the efficiency constant C used in Eq. (1). This formulation retains the original energy-based approach, introducing only two fitting exponents. Those exponents (−0.7 and −0.4 for the water-flow and air-flow scaling respectively) were determined by fitting the data. The scaling constant $\hat{C} = 1.12\times10^{-7}\ \mathrm{kg}^{1.1}/\mathrm{s}^{1.1}$ is likewise obtained by fitting the data. How these values relate to the flow dynamics surrounding the nozzle is unclear, given the complexity involved, but they are at least sufficiently accurate to represent the practical operating range of the sprayer as shown in Fig. 9.

5. Conclusions

The characteristics of a spray produced by a commercial external-mixing two-fluid electrostatic atomiser are experimentally investigated using the PDIA/shadowgraphy technique. The droplet size- and velocity distribution is determined at various distances from the nozzle, and the flow of air and liquid and the applied electric potential are varied. The used method yields good quality data for most of the operating range of the sprayer, although the number of recorded particles is reduced for cases with low mean droplet sizes and correspondingly high particle density.

The general behaviour of the sprayer in response to changes in air and liquid flow follows the pattern expected from theory. Droplet sizes increase with increasing liquid flow, and decrease with increasing air flow. The design of the sprayer suggests that the primary breakup mechanism is prompt atomisation, and the measured droplet size distribution is appropriate to this mechanism. However, unlike some other sprayer designs [16], the energy efficiency of the investigated nozzle decreases with increasing flowrates of both liquid and air. This can likely be contributed to the unconfined mixing region, leading to worse mixing at higher flowrates. Practically, it follows that more sprayers operating at lower flow rates use less energy than vice versa, for a given spray mass flow and droplet size distribution.

The voltage applied to the nozzle electrode appears to have no measurable influence on the spray properties. This confirms that aerodynamic effects are dominant in the atomisation region, as expected given that the pneumatic power supplied to the sprayer greatly exceeds the electrical power. It follows that any differences between the performance of charged and uncharged sprays (such as improved transfer efficiency) can be attributed to the charge of the droplets, rather than any other physical spray characteristics.

Declaration of competing interest

The authors declare that they have no known competing financial interests or personal relationships that could have appeared to influence the work reported in this paper.

Acknowledgement

This work is supported by the EFRO Oost-Nederland programme within the CrestCool project (# PROJ-00730).

References

[1] B. Hakberg, S. Lundqvist, B. Carlsson, T. Högberg, A theoretical model for electrostatic spraying and coating, J. Electrost. 14 (3) (1983) 255–268.
[2] Q. Ye, T. Steigleder, A. Scheibe, J. Domnick, Numerical simulation of the electrostatic powder coating process with a corona spray gun, J. Electrost. 54 (2) (2002) 189–205.
[3] A.G. Bailey, Electrostatic spraying of liquids, Phys. Bull. 35 (4) (1984) 146–148.
[4] G.W. Penney, Electrified Liquid Spray Dust Precipitator, Google Patents, 1944, US Patent 2, 357, 354.
[5] Instructions for adding electrostatic spray application directions for use to antimicrobial product registrations, EPA https://www.epa.gov/pesticide-registration/instructions-adding-electrostatic-spray-application-directions-use, (Accessed: 20 May 2021).
[6] J.W. Savell, S.L. Mueller, B.E. Baird, The chilling of carcasses, Meat Sci. 70 (3 SPEC. ISS.) (2005) 449–459.
[7] V.M. Allen, J.E.L. Corry, C.H. Burton, R.T. Whyte, G.C. Mead, Hygiene aspects of modern poultry chilling, Int. J. Food Microbiol. 58 (1–2) (2000) 39–48.
[8] A. Marchewicz, A.T. Sobczyk, A. Krupa, A. Jaworek, Induction charging of water spray produced by pressure atomizer, Int. J. Heat Mass Transfer 135 (2019) 631–648.
[9] A.H. Lefebvre, V.G. Mcdonell, Atomization and Sprays, second ed., CRC Press, Taylor and Francis, 2017, p. 300.
[10] T.C. Anestos, J.E. Sickles, R.M. Tepper, Charge to mass distributions in electrostatic sprays, IEEE Trans. Ind. Appl. IA-13 (April) (1977) 168–177.
[11] J.E. McCarthy, D.W. Senser, Specific charge measurements in electrostatic air sprays, Particul. Sci. Technol. 23 (1) (2005) 21–32.

[12] Q. Ye, J. Domnick, Analysis of droplet impingement of different atomizers used in spray coating processes, J. Coatings Technol. Res. 14 (2) (2017) 467–476.
[13] Q. Ye, K. Pulli, Numerical and experimental investigation on the spray coating process using a pneumatic atomizer: Influences of operating conditions and target geometries, Coatings 7 (1) (2017).
[14] A. Brentjes, A.K. Pozarlik, G. Brem, Numerical simulation of evaporating charged sprays in spray chilling, J. Electrost. 107 (September) (2020).
[15] J.L. Sallevelt, A.K. Pozarlik, G. Brem, Characterization of viscous biofuel sprays using digital imaging in the near field region, Appl. Energy 147 (2015) 161–175.
[16] A.H. Lefebvre, Energy considerations in twin-fluid atomization, Proc. ASME Turbo Expo 3 (January 1992) (1990) 89–96.
[17] T. Gemci, R. Hitron, N. Chigier, Determination of individual droplet charge in electrosprays from PDPA measurements, in: ILASS-Europe 2002, (September) 2002, pp. 1–6.
[18] R.T. Collins, J.J. Jones, M.T. Harris, O.A. Basaran, Electrohydrodynamic tip streaming and emission of charged drops from liquidcones, Nat. Phys. 4 (2) (2008) 149–154.
[19] W. Wei, Z. Gu, S. Wang, Y. Zhang, K. Lei, K. Kase, Numerical simulation of the cone-jet formation and current generation in electrostatic spray - Modeling as regards space charged droplet effect, J. Micromech. Microeng. 23 (1) (2013).
[20] J.S. Shrimpton, Y. Laoonual, Dynamics of electrically charged transient evaporating sprays, Internat. J. Numer. Methods Engrg. 67 (8) (2006) 1063–1081.
[21] LaVision, Particlemaster shadow: Product manual, 2017.
[22] A. Brentjes, A.K. Pozarlik, G. Brem, Estimating droplet charge in numerical simulations of charged sprays, J. Electrost. 112 (March) (2021) 103591.